

Model Order Reduction of Large-Scale Wind Farms: A Data-Driven Approach

Zilong Gong, Junyu Mao, Adrià Junyent-Ferré, *Senior Member, IEEE*, and Giordano Scarciotti, *Senior Member, IEEE*

Abstract—This paper proposes a data-driven algorithm for model order reduction (MOR) of large-scale wind farms and studies the effects that the obtained reduced-order model (ROM) has when this is integrated into the power grid. With respect to standard MOR methods, the proposed algorithm has the advantages of having low computational complexity and not requiring any knowledge of the high order model. Using time-domain measurements, the obtained ROM achieves the moment matching conditions at selected interpolation points (frequencies). With respect to the state of the art, the method achieves the so-called *two-sided* moment matching, doubling the accuracy by doubling the interpolated points. The proposed algorithm is validated on a combined model of a 200-turbine wind farm (which is reduced) interconnected to the IEEE 14-bus system (which represents the unreduced study area) by comparing the full-order model and the reduced-order model in terms of their Bode plots, eigenvalues and the point of common coupling voltages in extensive fault scenarios of the integrated power system.

Index Terms—wind farm model order reduction, moment matching, data-driven algorithm, low computational complexity.

I. INTRODUCTION

In recent years, there has been a significant increase in efforts to reduce the dependency on coal, petroleum, natural gas and other fossil fuels in order to overcome the effects of global warming. Society as a whole is motivated to replace traditional synchronous generators with renewable generations. In particular, wind farms, which are considered to be a clean, reliable and constant source of energy, are being deployed worldwide [1]. However, it is worth noting that in average more than 200 wind turbine generators (WTGs) are required to replace a single coal-fired power plant [2]. As a result, a detailed model of a large-scale wind farm typically contains thousands of differential equations. Such a detailed wind farm model can quickly become too complicated for further analysis, especially when hundreds of scenarios need to be simulated. These simulations are often time-consuming or even infeasible due to limited computational power. A solution to this problem is to find reduced models that capture the main dynamics of the large-scale wind farm in a substantially smaller number of differential equations while preserving the main properties (*e.g.* stability) of the whole interconnected power system. This problem is known as model order reduction (MOR). In the context of power systems, model order reduction is normally applied to a partition of the whole network. The idea is to distinguish between a study area, the description of which is

maintained in full detail, and an external area (*e.g.* an off-shore wind farm), consisting of the remaining part of the network, which is linearised and reduced. The study area can be precisely analysed and controlled while still considering the interaction of the interconnection of such area with a less faithful representation of a larger external area. This allows faster simulations of hundreds of scenarios in a fraction of the time, [3]–[6].

Several MOR methods have been successfully applied to large-scale wind farms. Historically, the most widely used one is the aggregation method [7]–[13], which simply assumes that all WTGs operate uniformly at the same wind speed and output power, and replaces all WTGs with a single aggregated WTG. However, given that large-scale wind farms are typically distributed over a large area, it is unrealistic to assume that the WTGs operate under the same conditions. To overcome this, one may use multiple aggregated WTGs to represent WTGs under different operating conditions. However, the implementation of this method in wind farms remains limited. Unlike classical generators, which can be easily classified into coherent groups by means of their physical characteristic (*e.g.* rotor angle), the criteria for classifying the WTGs remains unclear. Furthermore, the operating conditions of the wind farm change continuously, resulting in dynamic coherent groups over time.

Due to the above limitations, non-coherent based techniques have been considered for the reduction of wind farm models, such as Balanced Truncation (BT) [14]–[16], and Rational Krylov methods (RK) [16]–[18]. Some successful applications of BT and RK methods to power systems can be seen, for instance, in [19]–[22]. However, these methods have high computational complexity when reducing detailed wind farm models (*e.g.* some may require solving high dimensional Lyapunov equations). To improve this aspect, faster versions of these algorithms have been proposed, *e.g.* the Alternating Direction Implicit (ADI)-based Balanced Truncation [23] and the Iterative Rational Krylov Algorithm (IRKA) [24]. A detailed comparison of these methods is given in [4]. In addition to the high computational complexity, another weakness of these methods is that they require full information about the model (*i.e.* the system matrices A , B and C , see (1)), which is not a realistic assumption, especially in the case of large-scale wind farms. Wind farm model parameters are commonly owned by commercial companies and are not made available to the operators and users, who may have access only to a black-box model. Therefore, in practice effective MOR approaches should be *model free* or, in other words, *data-driven*. A successful application of a data-driven approach to power systems is [3], in which a benchmark model of 16 classical generators is

Zilong Gong, Junyu Mao, Adrià Junyent-Ferré and Giordano Scarciotti are with the Department of Electrical and Electronic Engineering, Imperial College London, London, SW7 2AZ, UK. {zilong.gong18, junyu.mao18, adria.junyent-ferre, g.scarciotti}@imperial.ac.uk.

reduced. In particular, [3] (see also [25] for the mathematical development) proposed a **one-sided** time-domain data-driven MOR algorithm based on moment matching. This approach allows selecting arbitrary “interpolation points” in the frequency domain such that the Bode plots of the full-order model (FOM) and of the reduced-order model (ROM) are matched at these particular frequencies. Some critical frequencies, which are important for analysis purposes and are strongly related to the mechanical and electrical characteristics of the power system are the so-called critical modes. Typically, critical modes are indicated by significant peaks in the magnitude of the Bode plot. Therefore, the moment matching approach has the notable advantage of enabling the preservation of the critical modes, thus maintaining some physical meaning while reducing the model.

In this paper, we propose a fully data-driven time-domain **two-sided** model reduction method for multiple input, multiple output (MIMO) systems. Moreover, the method is validated on a combined model of a 200-turbine wind farm (which represents the external area) and the IEEE 14-bus system (which represents the study area) in terms of Bode plots, eigenvalues, PCC (Point of Common Coupling) voltages and fault behaviour of the FOM and ROM. With respect to the techniques for model order reduction of wind farms available in the literature, the proposed method has the following key advantages and innovations.

- **Data-driven method.** This allows to apply the method even if the parameters of the wind farm are IP-protected and unknown to the user.
- **Low computational complexity.** Even when the model is available, the proposed method provides computational advantages with respect to model-based MOR. In this case synthetic data is generated in simulation by accurate or black-box models, and is noise free. We show that the execution of the proposed data-driven method has computational speed which is hundreds of times faster than the equivalent model-based method.
- **Robustness.** In practice, real measured data commonly contains measurement noise. Therefore, effective data-driven algorithms should be robust against noise. In the validation section (Section IV), we show a combination of comparisons with and without noise, to illustrate the advantages of the proposed method in both the real and synthetic data scenarios.
- **Two-sided.** The method achieves **two-sided** moment matching. By “two-sided” we mean that the number of interpolation points is *doubled* with respect to previously available methods (e.g. [3]). The implication is that for the same order, the ROM that we produce is as accurate as one with double its order. Alternatively, we can construct a ROM with the same number of interpolation points but with *half* the order.

The rest of the paper is organised as follows. In Section II, some preliminaries on moment matching are given. With a specific focus on MIMO systems, we introduce the moment matching conditions along tangential directions. In Section III, we propose data-driven algorithms for the MOR of MIMO

systems. In Section IV-A, we describe the combined model of the wind farm and the IEEE 14-bus system, the nonlinear model of the study area and the linearised model of the external area. In Section IV-B the external area is reduced and compared with the FOM in terms of the Bode plot, while in Section IV-C the robustness of the data-driven algorithms is assessed under noise conditions. In Section IV-D the ROM is reconnected to the study area and validated in terms of eigenvalues and the PCC voltage. In Section IV-E, the performance of the data-driven MOR method is evaluated by comparing the time required to construct the ROM and the time to execute a simulation. In Section IV-F, we analyse the fault behaviour of the FOM and ROM. In section V, we provide some concluding remarks. Finally, an Appendix provides the proofs of the theorems and an external reference containing the full detailed model, additional figures, and a working demo.

Notation: The symbols \mathbb{R} and \mathbb{C} denote the sets of real and complex numbers while the symbol \mathbb{Z} denotes the set of integer numbers. The identity matrix is denoted by I . The transpose of the matrix A is denoted by A^\top while the vectorization of the matrix A is denoted by $\text{vec}(A)$. $\sigma(A)$ denotes the spectrum of the matrix $A \in \mathbb{R}^{n \times n}$. $\|\cdot\|$ denotes the induced Euclidean matrix norm and $\delta_0(t)$ denotes the delta-Dirac impulse. $0_{m \times n}$ represents the $m \times n$ zero matrix. The symbol e_j denotes the j -th vector of the standard basis (i.e. $\underbrace{[0 \cdots 0, 1, 0 \cdots 0]^\top}_j$).

II. PRELIMINARIES - MODEL-BASED MOMENT MATCHING

In this section we recall the model-based moment matching method for linear MIMO systems. We first recall a family of ROMs matching ν so-called right interpolating conditions, then a family of ROMs matching ν so-called left interpolating conditions, and then show how to obtain a ROM that matches 2ν interpolating conditions.

A. Right Interpolation \equiv Direct Interconnection

Consider a linear MIMO continuous-time system

$$\dot{x} = Ax + Bu, \quad y = Cx, \quad (1)$$

where $x(t) \in \mathbb{R}^n$ is the state, $u(t) \in \mathbb{R}^m$ is the input, $y(t) \in \mathbb{R}^p$ is the output, $A \in \mathbb{R}^{n \times n}$, $B \in \mathbb{R}^{n \times m}$, $C \in \mathbb{R}^{p \times n}$ are the system matrices. Without loss of generality system (1) is assumed to be the minimal realisation of the transfer matrix $W(s) = C(sI - A)^{-1}B$. We now introduce the definition of moments.

Definition 1. Let $s_i \in \mathbb{C} \setminus \sigma(A)$ and $l_i \in \mathbb{R}^m$. The k -moment of system (1) along l_i is a vector defined as $\eta_k(s_i, l_i) = \frac{(-1)^k}{k!} \left[\frac{d^k}{ds_i^k} W(s_i) \right] l_i$, for $k \geq 0$ integer.

The quantities s_i are called interpolation points, while the quantities l_i are called right tangential directions.

The idea of MOR by moment matching is to construct a ROM with transfer function $\hat{W}(s)$ (and k -moment along l_i called $\hat{\eta}_k(s_i, l_i)$) that, for ν interpolation points s_i , satisfies the right side moment matching condition, namely

$$\eta_k(s_i, l_i) = \hat{\eta}_k(s_i, l_i), \quad \text{for } i = 1, \dots, \nu. \quad (2)$$

This problem is readily solved as follows: let $S \in \mathbb{R}^{\nu \times \nu}$ be any matrix with characteristic and minimal polynomials $p(s) = \prod_{i=1}^{\bar{k}} (s - s_i)^{k_i}$, where $\nu = \sum_{i=1}^{\bar{k}} k_i$, and $L = [l_1, l_2, \dots, l_\nu] \in \mathbb{R}^{m \times \nu}$, any matrix such that (S, L) is an observable pair. Then, the family of models

$$\dot{\xi} = (S - GL)\xi + Gu, \quad \psi = C\Pi\xi, \quad (3)$$

achieves moment matching at the interpolation points encoded by S along the directions encoded by L , for any $G \in \mathbb{R}^{\nu \times m}$ such that $\sigma(S) \cap \sigma(S - GL) = \emptyset$, as long as L is selected as in [26, Section 2.4] (e.g. $l_i = l \neq 0_{m \times 1}$ for all i). The quantity Π in (3) is the unique solution of the Sylvester equation

$$A\Pi + BL = \Pi S. \quad (4)$$

It is important to notice for the sake of the data-driven algorithms that we develop in this paper, that the quantity $C\Pi\omega(t)$ is the steady-state output y_{ss} of system (1) interconnected (see Fig. 1) with the input produced by the generator

$$\dot{\omega} = S\omega, \quad u = L\omega. \quad (5)$$

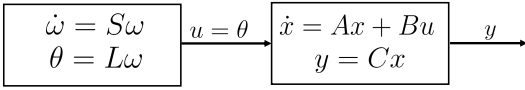


Fig. 1. The diagram of the direct interconnection.

B. Left Interpolation \equiv Swapped Interconnection

The same approach can be developed for the so-called left-side interpolation data.

Definition 2. Let $q_i \in \mathbb{C} \setminus \sigma(A)$ (interpolation points) and $r_i \in \mathbb{R}^{1 \times m}$ (left tangential directions). The k -moment of system (1) along r_i is a vector defined as $\mu_k(q_i, r_i) = r_i \frac{(-1)^k}{k!} \left[\frac{d^k}{dq_i^k} W(q_i) \right]$, for $k \geq 0$ integer.

Similarly to before, we now want to find a ROM with moments $\hat{\mu}_k(q_i, r_i)$, such that

$$\mu_k(q_i, r_i) = \hat{\mu}_k(q_i, r_i), \quad \text{for } i = 1, \dots, \nu. \quad (6)$$

Also this problem is readily solved: let $Q \in \mathbb{R}^{\nu \times \nu}$ be any matrix with characteristic and minimal polynomials $p(q) = \prod_{i=1}^{\bar{k}} (q - q_i)^{k_i}$, where $\nu = \sum_{i=1}^{\bar{k}} k_i$, and $R = [r_1^\top, r_2^\top, \dots, r_\nu^\top]^\top \in \mathbb{R}^{\nu \times p}$, any matrix such that (Q, R) is a reachable pair. Then, the family of models

$$\dot{\xi} = (Q - RH)\xi + \Upsilon Bu, \quad \psi = H\xi, \quad (7)$$

achieve moment matching at the interpolation points encoded by Q along the direction encoded by R , for any $H \in \mathbb{R}^{p \times \nu}$ such that $\sigma(Q) \cap \sigma(Q - RH) = \emptyset$, as long as R^\top is selected as

in [26, Section 2.4] (e.g. $r_i = r \neq 0_{1 \times p}$ for all i). The quantity Υ in (7) is the unique solution of the Sylvester equation

$$\Upsilon A + RC = Q\Upsilon, \quad (8)$$

It is important to notice (see [27]) for the sake of the data-driven algorithms that we develop in this paper, that **for SISO systems** the quantity $e^{Qt}\Upsilon B$ is the output d or steady-state of ϖ of the system

$$\dot{\varpi} = Q\varpi + Ry, \quad d = \varpi + \Upsilon x, \quad (9)$$

that filters the output impulse response of system (1), that is $d(t) = \varpi_{ss}(t) = e^{Qt}\Upsilon B$ (see Fig. 2). In this paper, we prove these properties **for MIMO systems**.

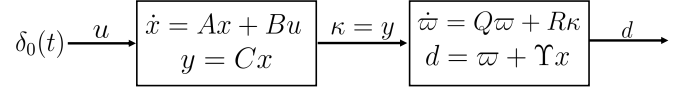


Fig. 2. The diagram of the swapped interconnection.

C. Concurrent Left and Right Interpolation \equiv Two-sided Interconnection

The ROM (3) [(7) respectively] are of order ν and match ν right [left] interpolation condition while they have a free G [H]. It is possible to select G [H] in such a way that also the left [right] interpolation conditions are satisfied (assuming that these conditions are different, i.e. $\sigma(S) \cap \sigma(Q) = \emptyset$). In particular, the ROM (3) [(7)] with

$$G = (\Upsilon\Pi)^{-1}\Upsilon B, \quad [H = C\Pi(\Upsilon\Pi)^{-1}]$$

matches both left and right interpolation data (see [28]). Thus the obtained reduced-order model of order ν matches 2ν moments. It is important to notice for the sake of the data-driven algorithms that this setup corresponds to the two-sided interconnection shown in Fig. 3 for which the steady-state property $d_{ss}(t) - \varpi_{ss}(t) = \Upsilon\Pi\omega(t)$ holds.



Fig. 3. The diagram of the two-sided interconnection.

The idea of the method presented in this paper is to use time series of the outputs of these interconnections to generate a two-sided reduced-order model without solving (4) and (8) or using A , B and C .

III. DATA-DRIVEN MODEL ORDER REDUCTION

One can see that the ROMs proposed in (3) and (7) rely on the unique solutions of the Sylvester equations (4) and (8) respectively. Since these Sylvester equations involve $n \times \nu$ conditions, if n is large they are computationally challenging to solve. This results in high computational complexity when implementing this approach to wind farms which are commonly large-scale. Furthermore, as mentioned in Section I, detailed

information of the system matrices (*i.e.* A , B and C) of large-scale wind farms may not be available. Thus, we are motivated to find a data-driven MOR approach that requires input-output data only.

A data-driven algorithm for two-sided MOR of SISO systems has been proposed in [29]. However, large-scale wind farms are commonly modeled with multiple inputs and multiple outputs (*i.e.* voltages and currents in dq framework). Thus, a MIMO method is required. The main difficulty of the MIMO case is that we cannot directly match all quantities of the transfer matrix $W(s)$ because for a matrix $W(s)$ of dimension m (inputs) by p (outputs) and ν interpolation points, then $mp\nu$ interpolation conditions need to be satisfied, whereas the degrees of freedom of $C\Pi$ are only $p\nu$. Therefore, we merge the $mp\nu$ conditions into just $p\nu$ by using tangential directions as in Definition 1 and Definition 2. A data-driven algorithm for *one-sided* MOR of MIMO systems was presented in [3]. Here we propose a novel algorithm for *two-sided* MOR of MIMO systems, thus producing ROMs with double the accuracy of the method¹ given in [3].

From Section II we have seen that a reduced-order model by moment matching that achieved two-sided interpolation can be constructed as

$$\dot{\xi} = (S - (\Upsilon\Pi)^{-1}\Upsilon BL)\xi + (\Upsilon\Pi)^{-1}\Upsilon Bu, \quad \psi = C\Pi\xi, \quad (10)$$

if we have the matrices $C\Pi$, ΥB and $\Upsilon\Pi$. Therefore, the data-driven approach consists in finding accurate approximations $\widetilde{C\Pi}$, $\widetilde{\Upsilon B}$ and $\widetilde{\Upsilon\Pi}$ from data.

A. Constructing $\widetilde{C\Pi}$

Consider the experimental setup in Fig. 1 or Fig. 3 in which the system is excited with inputs produced by the generator (5). Samples of the output $y(t_i)$ of the system are collected together with $\omega(t_i)$ (the latter can be collected or computed exactly). Then the following theorem (see Appendix A for the proof) provides a formula to estimate $C\Pi$. The theorem provides convergence guarantees for Algorithm 1.

Theorem 1. Consider the interconnection of system (1) and the signal generator (5). Assume $\sigma(A) \subset \mathbb{C}_{<0}$, $\sigma(S) \subset \mathbb{C}_0$, S has simple eigenvalues and the triple $(L, S, \omega(0))$ is minimal. For $\tilde{\nu} \geq \nu$, define the time-snapshots $\widetilde{R}_k \in \mathbb{R}^{\tilde{\nu} \times \nu}$ and $\widetilde{E}_k^j \in \mathbb{R}^{\tilde{\nu}}$ as

$$\begin{aligned} \widetilde{R}_k &= [\omega(t_{k-\tilde{\nu}+1}) \cdots \omega(t_{k-1}) \ \omega(t_k)]^\top, \\ \widetilde{E}_k^j &= [y^j(t_{k-\tilde{\nu}+1}) \cdots y^j(t_{k-1}) \ y^j(t_k)]^\top, \end{aligned}$$

where $y^j(t_i)$ is the j -th row of $y(t_i)$. Denote the j -th row of C as C^j . Then,

$$\text{vec} \left(\widetilde{C^j\Pi_k} \right) = (\widetilde{R}_k^\top \widetilde{R}_k)^{-1} \widetilde{R}_k^\top \widetilde{E}_k^j. \quad (11)$$

is an *online estimate* of $C^j\Pi$, which is the j -th row of $C\Pi$, namely there exists a sequence $\{t_k\}$ such that $\widetilde{R}_k^\top \widetilde{R}_k$ is full rank and $\lim_{k \rightarrow \infty} \widetilde{C^j\Pi_k} = C^j\Pi$.

¹There is also a difference in the MIMO aspect with respect to [3]. In [3], a heuristic was used to determine L , producing only *approximate* one-sided moment matching. Here, L and R are selected based on the recent results in [26]. The resulting ROM is not an approximation.

Algorithm 1 Approximate $C\Pi$

Input: A sufficiently large integer $k_0 \in \mathbb{Z}_{>0}$ and sufficiently small error thresholds $\eta_{C\Pi}^j > 0$, with $j = 1, \dots, p$. Let $\tilde{\nu} = \nu$ (increase $\tilde{\nu}$ sufficiently for robustness).

- 1: **for** $j = 1$ to p **do**
 - 2: Let $k = k_0$.
 - 3: Construct the matrices \widetilde{R}_k and \widetilde{E}_k^j .
 - 4: **if** $\text{rank}(\widetilde{R}_k) = \nu$ **then**
 - 5: Compute $\widetilde{C^j\Pi_k}$ from equation (11).
 - 6: **if** $\frac{\|C^j\Pi_k - C^j\Pi_{k-1}\|}{t_k - t_{k-1}} > \eta_{C\Pi}^j$ **then**
 - 7: $k = k + 1$ go to 3.
 - 8: **end if**
 - 9: **else**
 - 10: Increase $\tilde{\nu}$ go to 3.
 - 11: **end if**
 - 12: **return** $\widetilde{C^j\Pi_k}$.
 - 13: **end for**
 - 14: **return** $\widetilde{C\Pi_k}$.
-

Algorithm 1 can be made robust against measurement noise. It is enough to pick a larger $\tilde{\nu}$. This variant gives the optimal estimation (*i.e.* maximum likelihood estimation) of $C^j\Pi$ when the measurements are affected by Gaussian additive noise.

B. Constructing $\widetilde{\Upsilon B}$

Consider the experimental setup in Fig. 2 in which the output impulse response of system (1) is filtered by (9). Samples of the filtered state $\varpi(t_i)$ are collected together with the quantities e^{Qt_i} (these can be computed exactly). Then the following theorem (see Appendix A for the proof) provides a formula to estimate ΥB .

Theorem 2. Consider the interconnection of system (1) and (9). Assume $\sigma(A) \subset \mathbb{C}_{<0}$, $\sigma(Q) \subset \mathbb{C}_0$, Q has simple eigenvalues and the pair (Q, R) is reachable. Denote the j -th column of B as B^j . Let the initial conditions $x(0) = 0$ and $\varpi(0) = 0$, and the input of the j -th experiment $u_j = e_j\delta_0(t)$. Then

$$\widetilde{\Upsilon B}_k^j := e^{-Qt_k} \varpi(t_k) \quad (12)$$

is an online estimate of ΥB^j with the following asymptotic property: there exists a time sequence $\{t_k\}$ such that $\lim_{k \rightarrow \infty} \widetilde{\Upsilon B}_k^j = \Upsilon B^j$.

Equation (12) can be made robust against measurement noise. To this end we replace (12) with

$$\text{vec} \left(\widetilde{\Upsilon B}_k^j \right) = (\widetilde{P}_k^\top \widetilde{P}_k)^{-1} \widetilde{P}_k^\top \widetilde{O}_k^j, \quad (13)$$

where $\widetilde{O}_k^j \in \mathbb{R}^{\tilde{q}\nu}$ and $\widetilde{P}_k \in \mathbb{R}^{\tilde{q}\nu \times \nu}$ are defined as

$$\begin{aligned} \widetilde{O}_k^j &= [\varpi(t_{k-\tilde{q}+1})^\top \cdots \varpi(t_{k-1})^\top \ \varpi(t_k)^\top]^\top, \\ \widetilde{P}_k &= [e^{Qt_{k-\tilde{q}+1}} \cdots e^{Qt_{k-1}} \ e^{Qt_k}]^\top, \end{aligned}$$

and note that \widetilde{P}_k is always full column rank. For a sufficiently large number \tilde{q} , this variant gives the optimal estimation (*i.e.*

maximum likelihood estimation) of ΥB^j when the measurements are affected by Gaussian additive noise. The results of this section are summarised in Algorithm 2.

Algorithm 2 Approximate ΥB

Input: A sufficiently large integer $k_0 \in \mathbb{Z}_{>0}$ and sufficiently small error thresholds $\eta_{\Upsilon B}^j > 0$ with $j = 1, \dots, m$. Let $\tilde{q} = 1$ (increase \tilde{q} sufficiently for robustness).

- 1: **for** $j = 1$ to m **do**
- 2: Let $k = k_0$.
- 3: Produce the data with the input $u_j = e_j \delta_0(t)$.
- 4: Construct the matrices \tilde{O}_k^j and \tilde{F}_k .
- 5: Compute $\tilde{\Upsilon B}_k^j$ from equation (13).
- 6: **if** $\frac{\|\tilde{\Upsilon B}_k^j - \tilde{\Upsilon B}_{k-1}^j\|}{t_k - t_{k-1}} > \eta_{\Upsilon B}^j$ **then**
- 7: $k = k + 1$ go to 4.
- 8: **end if**
- 9: **return** $\tilde{\Upsilon B}_k^j$.
- 10: **end for**
- 11: **return** $\tilde{\Upsilon B}_k$.

C. Constructing $\tilde{\Upsilon \Pi}$

Provided with satisfying approximations $\tilde{C \Pi}_k$ and $\tilde{\Upsilon B}_k$, we are left with the problem of estimating $\Upsilon \Pi$ from data. For SISO systems, [29] proposed a third algorithm based on an additional experiment and the use of a ‘‘surrogate’’ system (see [29] for details). Here we present an alternative method (for both SISO and MIMO systems) that has the advantage of not requiring a third experiment and algorithm.

By multiplying equation (4) from the left by Υ , and equation (8) from the right by Π and matching the resulting common terms $\Upsilon A \Pi$, yield the new equation

$$Q \Upsilon \Pi - \Upsilon \Pi S = R C \Pi - \Upsilon B L.$$

Exploiting the approximations $\tilde{C \Pi}_k$ and $\tilde{\Upsilon B}_k$, we can find an approximation of $\Upsilon \Pi$ by solving the Sylvester equation

$$Q \tilde{\Upsilon \Pi}_k - \tilde{\Upsilon \Pi}_k S = R \tilde{C \Pi}_k - \tilde{\Upsilon B}_k L \quad (14)$$

with respect to $\tilde{\Upsilon \Pi}_k$. This equation has a unique solution as long as Q and S have no common eigenvalues. Since Q and S are arbitrary, this is not a restriction. Moreover, note that differently from the Sylvester equations (4) and (8) that correspond to n by ν and ν by n scalar equations, respectively, the Sylvester equation (14) only involves ν by ν scalar equations. Since $\nu \ll n$, the computational complexity of solving (14) is small and does not need to be avoided as it was the case for (4) and (8).

D. Algorithmic Overview

The complete method is summarised as a flowchart in Fig. 4. Once the study and external areas are given, we determine a linearised model of the external area. The next step consists in selecting the number and location of the interpolation points and the corresponding tangential directions for the right and left side moment matching. These parameters, which determine

the performance of the ROM, can be selected based on user’s knowledge of the wind farm or its operating conditions, or by using a fast Fourier transform on available data to determine the frequencies of interest to be interpolated. We generate the data $y(t)$, $\omega(t)$, and $\varpi(t)$, and compute $\tilde{C \Pi}_k$ and $\tilde{\Upsilon B}_k$ by Algorithm 1 and Algorithm 2 respectively. $\tilde{\Upsilon \Pi}_k$ is obtained by solving (14). Finally, the two-sided reduced-order model is given by (10). If the resulting ROM is not satisfactory, we return to the step of selecting the interpolation points and the corresponding tangential directions. Otherwise, we stop. A demo of the method is available in Appendix C.

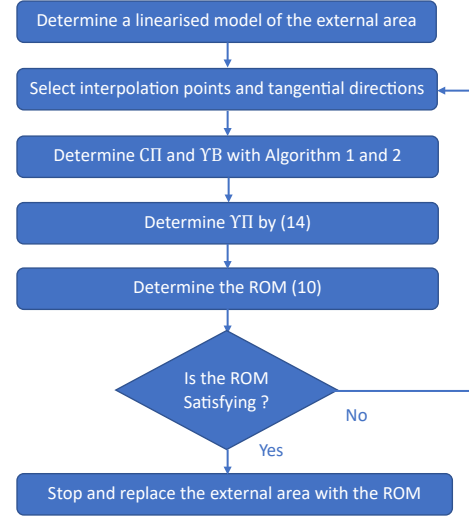


Fig. 4. Algorithmic overview of the method

IV. APPLICATION TO THE WIND FARMS

In this section we present extensive simulation results to validate the proposed method. After introducing the wind farm model used in this work (Section IV-A) and the obtained ROM (Section IV-B), we first evaluate the robustness of the data-driven algorithms to measurement noise (Section IV-C) and then compare the FOM and the ROM in terms of eigenvalues, PCC voltage, computational time and fault behaviour (Sections IV-D, IV-E, IV-F).

A. Combined system: wind farm and IEEE 14-bus system

To validate our MOR approach, we consider a $200 \times 1\text{MW}$ wind farm of type-4 wind turbine generators (WTGs) in a 50Hz power system. The basic layout of the combined system is shown in Fig. 5. The wind farm consists of 20 strings, where each string contains 10 WTGs, while the rest of the power system consists of 14 buses, 5 synchronous generators, 11 loads and 20 transmission lines (see [30] for more detail). The wind farm is connected to the Bus 7. In Fig. 5, each triangle represents a WTG connected to a wind turbine transformer (WTT). The dynamic model of a single WTG has order 9 (see e.g. [31]), which increases to 17 once connected with the transformer and cable. The full detailed model, including all the parameters used in this study, is provided in [30].

The large-scale wind farm and the IEEE 14-bus system are modelled using Matlab/Simulink. We define the study area and the external area as shown in Fig. 5. The study area is preserved while the external area is linearised using the linearisation toolbox in Matlab/Simulink (note that linearisation is common in this context, see *e.g.* [4], [6]). The resulting model of the external area has an order of 3402 with 1592 conjugate pairs of eigenvalues. This linear FOM of the external area includes two inputs and two outputs, namely the current at the wind farm transformer (WFT) on the qd -axis and the PCC voltage on the qd -axis, respectively. The FOM of the external area is subsequently reduced by our data-driven approach and reconnected to the study area for comparison and validation against the FOM. In the rest of the section, this combined system is simulated in Simulink using ‘variable-step’ with a max step size of 5.5×10^{-6} . Note that for the purpose of model order reduction, no parameters or system matrices are used. Only the data as defined in the data-driven algorithms are used. The matrices are used only for validation purposes.

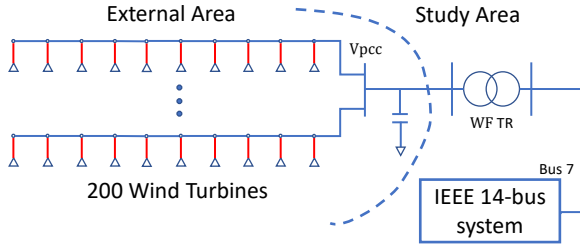


Fig. 5. The layout of the combined system. A fully detailed model is provided in [30].

B. Design of the reduced-order model

Following the development of Section III, we implement Algorithm 1, Algorithm 2 and solve² (14), finding estimations of $C\Pi$, ΥB and $\Upsilon\Pi$, respectively. The first step is to determine the interpolation points and the corresponding tangential directions for moment matching. In this example, the interpolation points are selected by spreading them between the frequencies of 0Hz and 10000Hz, placing some of these frequencies³ in S and some in Q . Specifically, we used $\pm 1\iota$, $\pm 20\iota$, $\pm 70\iota$, $\pm 120\iota$, $\pm 300\iota$, $\pm 500\iota$, $\pm 700\iota$, $\pm 900\iota$, $\pm 4400\iota$ and $\pm 8500\iota$ for Algorithm 1 and $\pm 10\iota$, $\pm 50\iota$, $\pm 100\iota$, $\pm 200\iota$, $\pm 400\iota$, $\pm 600\iota$, $\pm 800\iota$, $\pm 1000\iota$, $\pm 7000\iota$ and $\pm 10000\iota$ for Algorithm 2. We select the tangential directions according to [26] as $l_i = [1, 4]^T$ and $r_i = [4, 1]$ for all $i = 1, \dots, \nu$ for the direct and swapped moment matching, respectively. The performance of the data-driven algorithms is evaluated by the normalised approximation error defined as

$$e_x = \frac{\|\tilde{x}_k - x\|}{\|x\|},$$

²Using the function ‘sylvester’ in Matlab.

³It may not always be possible to arbitrarily select the input of system (1) as in Fig. 1 and Fig. 2, and in reality the input signal may be composed of several unwanted frequencies. For this case, one can use a band-pass filter and apply the algorithms to the filtered data, as suggested for instance in [25, Remark 2].

where x is any quantity required to construct the ROM (*i.e.* $C\Pi$, ΥB and $\Upsilon\Pi$) and \tilde{x}_k is the corresponding approximation given by the data-driven algorithm (*i.e.* $\widehat{C\Pi}_k$, $\widehat{\Upsilon B}_k$ and $\widehat{\Upsilon\Pi}_k$). The system is simulated for 100 seconds to generate sufficient data⁴ for the two algorithms. This yields sufficiently small normalised approximation errors $e_{C\Pi} = 2.1 \times 10^{-6}$ and $e_{\Upsilon B} = 8.8 \times 10^{-4}$. Once satisfactory approximations of $C\Pi$ and ΥB are obtained, we solve equation (14) to estimate $\Upsilon\Pi$, yielding a normalised approximation error of $e_{\Upsilon\Pi} = 1.2 \times 10^{-6}$. Provided with approximations $\widehat{C\Pi}_k$, $\widehat{\Upsilon B}_k$ and $\widehat{\Upsilon\Pi}_k$, the ROM of order $\nu = 20$ is given by (10).

Fig. 6 and Fig. 7 compare the Bode plots for the right- and left-side moment matching, respectively. In particular, the blue solid lines represent quantities related to the FOM, the black dotted lines represent quantities related to the model-based ROM and the dashed red lines represent quantities related to the data-driven ROM. The figures show that the selection of the interpolation points is effective and the transfer matrix along the tangential directions is perfectly matched. Hence, the performance of the model-based reduced-order model is fully recovered by the data-driven approach. In Fig. 8, the Bode plot of the FOM and ROMs (model-based and data-driven) are represented by solid blue, black dotted and red dashed lines, respectively. Note that while there is no guarantee that the transfer matrix is well matched (the guarantee is along the left and right directions only), the figure clearly shows that the transfer matrix itself is well matched across all the considered frequencies.

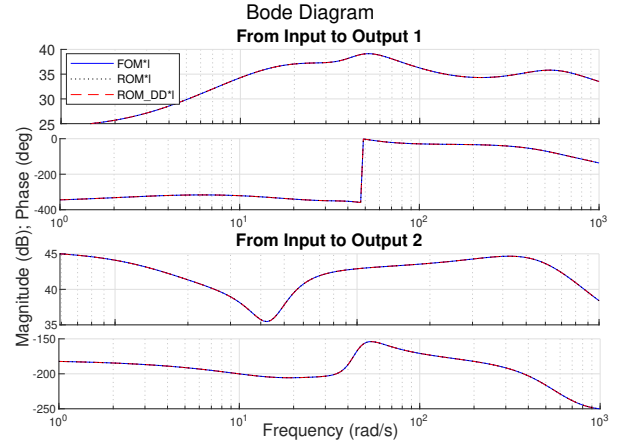


Fig. 6. Bode plot of the right side moment matching along the tangential direction l . The solid blue line, black dotted line and red dashed line represent the quantities for the FOM, ROM (model-based) and ROM_DD (data-driven), respectively.

Furthermore, to illustrate the two-sided property, the proposed method is compared with the one-sided method given by [3]. Since the FOM in this example has two inputs and two outputs, the moments along the tangential directions consist of two transfer functions (see Definition 1 and Definition 2). The values of the first and second transfer function at the required interpolation points are presented with blue stars

⁴In practice, the required data can be collected by the phase measurement unit (PMU). In this paper, the data is obtained directly from simulations.

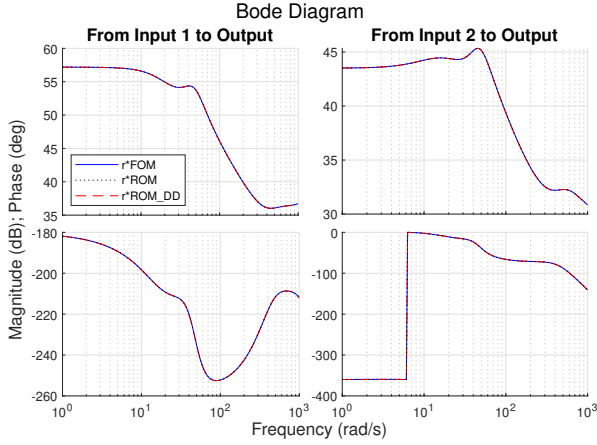


Fig. 7. Bode plot of the left side moment matching along the tangential direction r . The solid blue line, black dotted line and red dashed line represent the quantities for the FOM, ROM (model-based) and ROM_DD (data-driven), respectively.

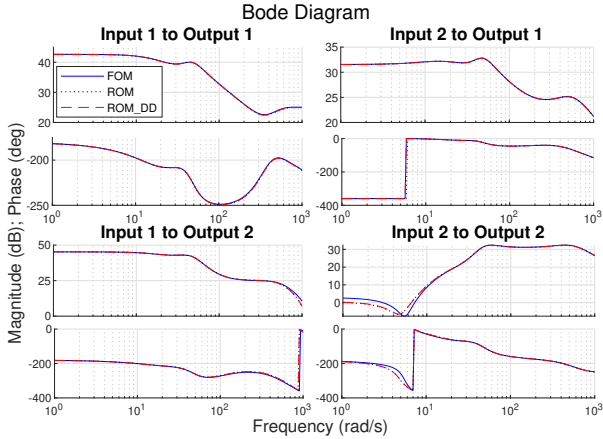


Fig. 8. Bode plot of the FOM and ROMs. The solid blue line, black dotted line and red dashed line represent the FOM, ROM (model-based) and ROM_DD (data-driven), respectively.

in Fig. 9 and Fig. 10, respectively. These figures confirm that for the constructed ROMs (represented by red circles for the two-sided method and black diamonds for the method in [3]) of the same order 20, the proposed two-sided method ensures double interpolations. In fact, the two-sided method achieves moment matching at all 40 interpolation points (all blue stars are surrounded by red circles), while the one-sided method achieves the moment matching at 20 interpolation points only (20 black diamonds surround 20 blue stars, but other 20 diamonds are empty, meaning that 20 prescribed interpolation points are missed).

In conclusion, in terms of quality of matching, the performance of the data-driven algorithm in absence of noise is satisfactory and equivalent to a model-based method. It is important to stress that this result is very valuable even when the model of the system is available and noiseless data is generated by means of simulations because, as shown later in Section IV-E, the data-driven method produces a reduced-order model in much less computational time than the model-based

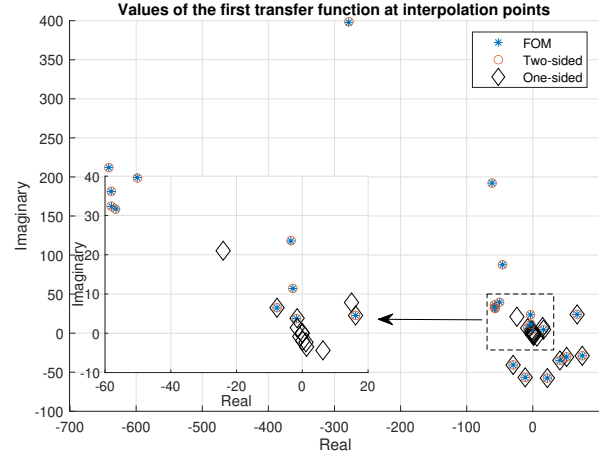


Fig. 9. Interpolation conditions for the first component of the transfer matrix. The blue stars, red circles and black diamonds represent the quantities related to the FOM, ROM (two-sided) and ROM (one-sided), respectively.

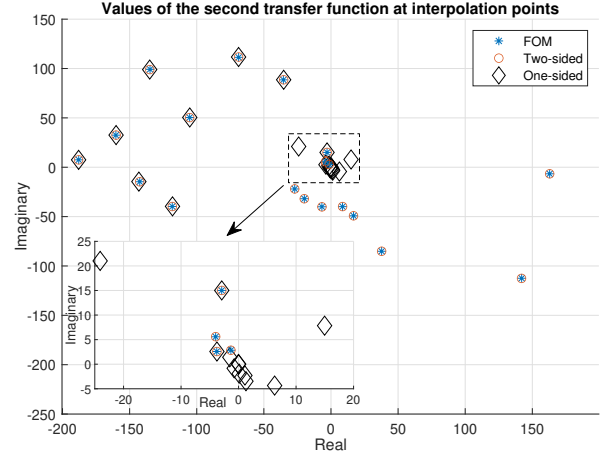


Fig. 10. Interpolation conditions for the second component of the transfer matrix. The blue stars, red circles and black diamonds represent the quantities related to the FOM, ROM (two-sided) and ROM (one-sided), respectively.

approach. Nevertheless, we study the robustness of the data-driven method to measurement noise in the next section.

C. Robustness against measurement noise

To evaluate the robustness of the proposed data-driven algorithm, we add Gaussian noise to the measurements of $\varpi(t)$. We consider 20 realisations of the noise with signal-noise-ratio (SNR) of 60dB, and we estimate the quantity ΥB both by the robust (Algorithm 2) and the non-robust (Theorem 2) method⁵. The average of $e_{\Upsilon B}$ over 20 realisations is denoted as $\bar{e}_{\Upsilon B}^r$ for the robust and $\bar{e}_{\Upsilon B}$ for the non-robust estimation. The corresponding average of $e_{\Upsilon \Pi}$ is denoted as $\bar{e}_{\Upsilon \Pi}^r$ and $\bar{e}_{\Upsilon \Pi}$, respectively. The robust algorithm (Algorithm 2) uses 1000 measurements, while the non-robust method (Theorem 2) uses only one measurement (the last). The robust estimations

⁵We have carried out the same analysis adding noise to $y(t)$ and studying the robustness of Algorithm 1 to estimate CII (using sufficiently large \bar{d}). The performance of Algorithm 1 and Algorithm 2 under a larger level of noise (*i.e.* 40dB) is also evaluated. These results are analogous and thus they are omitted for the reason of space. However, these can be found in [30].

have small averaged errors, *i.e.* $\bar{e}_{\Upsilon B}^r = 3.2 \times 10^{-5}$ and $\bar{e}_{\Upsilon \Pi}^r = 5.3 \times 10^{-5}$, while the non-robust estimations present averaged errors two orders of magnitude higher, namely $\bar{e}_{\Upsilon B} = 1.0 \times 10^{-3}$ and $\bar{e}_{\Upsilon \Pi} = 1.4 \times 10^{-3}$, respectively. Fig. 11 shows the regions between the upper and lower envelopes of all obtained magnitude plots of the ROMs obtained for the 20 realisations of the noise. In particular, the red regions refer to the robust estimation (Algorithm 2), the blue regions refer to the non-robust estimation (Theorem 2) and the brown dashed lines represent the ideal estimation (no noise). This figure confirms that the proposed data-driven algorithm (Algorithm 2) is robust with respect to measurement noise as, for \tilde{q} sufficiently large, the red regions are not only significantly smaller than the blue regions, but they are also close to the ideal case.

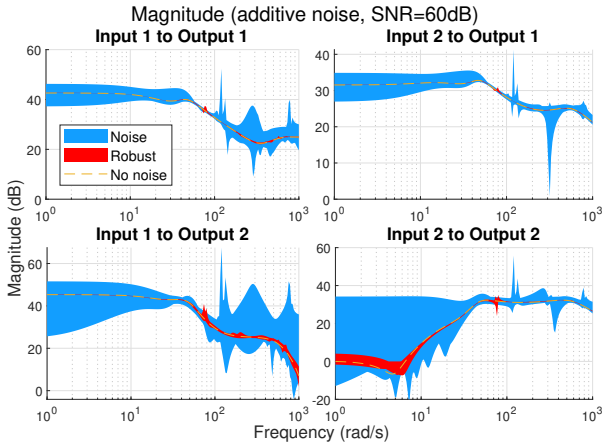


Fig. 11. Magnitude plots of the reduced-order models under 20 realizations of additive Gaussian noise. The red regions, blue regions and brown dashed lines refer to the robust algorithm (Algorithm 2), non-robust method (Theorem 2) and the ideal estimation (no noise), respectively.

D. Initial validation: stability and PCC voltage

In the two-sided approach, the free parameter G is used to double the number of interpolation points (See Section II-C and (10)). We select the interpolation points (encoded by S) and tangential directions L such that the ROM is stable. For further validation, we first compare the eigenvalues of the ROM and FOM and then we reconnect them with the study area to compare the PCC voltage. In Fig. 12, the eigenvalues of the FOM are represented by blue stars while the eigenvalues of the ROM obtained by the data-driven MOR method are illustrated by hollow red circles. The figure shows that the obtained ROM is stable and that the eigenvalues of the ROM have a similar spread as those of the FOM. Fig. 13 compares the PCC voltage of the FOM and ROM when they are reconnected to the study area. The top plot shows the PCC voltages in per-unit (with $V_{base} = 66kV$), whereas the bottom plot shows the relative error in percentage. The relative error of the PCC voltage decreases to less than 0.3% within 0.1s. Hence, the simulations confirm that the ROM can accurately recover the performance of the FOM in a short time.

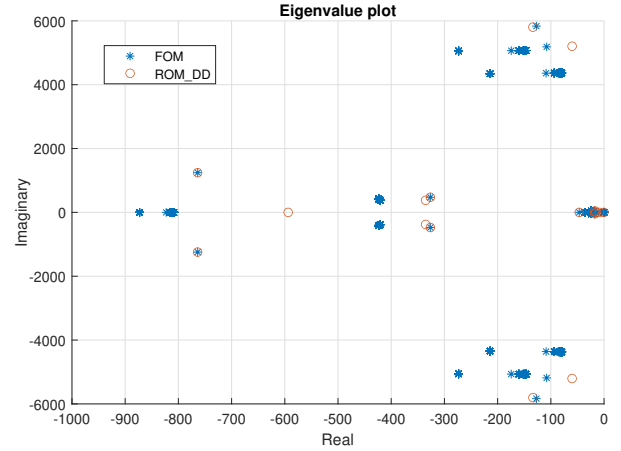


Fig. 12. Eigenvalues of the FOM and ROM_DD (data-driven), represented by the blue stars and hollow red circles, respectively.

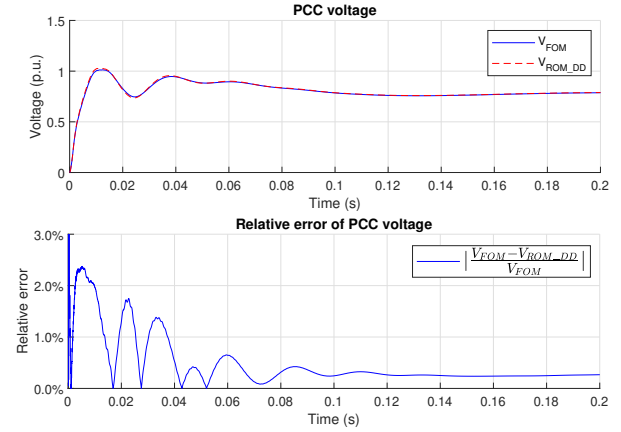


Fig. 13. Top: PCC voltage of the FOM and ROM_DD (data-driven), represented by solid blue and dashed red lines, respectively. Bottom: corresponding relative error.

E. Comparison of computational time

In order to evaluate the advantages of the data-driven MOR approach proposed in this paper, we compare the computational time of four wind farm models: 1) the nonlinear FOM (of the external area), 2) its linearisation, 3) the ROM constructed by solving the Sylvester equation (*i.e.* model-based method) and 4) the ROM constructed by the proposed data-driven approach. In addition, to show that the proposed data-driven method is advantageous in the synthetic data scenario, we compare also the “extraction time” of the MOR (that is, the time required to construct the ROM) for the data-driven method and the model-based method. Recall that the FOM of the wind farm has order 3402. The two ROMs have order 20.

Table I compares the computational time of the four models in terms of “extraction time” of the MOR and “elapsed time” of a 1 second simulation of the wind farm. All the simulations and MOR algorithms are run in Matlab/Simulink R2023b on the same personal laptop (Windows 10, Intel Core i7-10750H and 16GB RAM). The table shows that to perform a simulation of 1 second, the nonlinear FOM requires 1268.26 seconds (about 21 minutes), whereas the linearised FOM requires 796.31

seconds (about 13 minutes), which is time-consuming. By reducing the order of the model from 3402 to 20, the elapsed time is significantly reduced to around 1.5 seconds for both the model-based ROM and the data-driven ROM. While the elapsed time of the two ROMs is similar, the two methods show a stark difference in the extraction time, which reflects the computational complexity of the MOR methods. In fact, to construct a ROM of order 20 using a model-based approach requires 28.60 seconds, whereas using the data-driven method takes only 0.10 seconds. In summary, a simulation using the data-driven ROM is 530 times faster than a simulation using the linearised FOM, and this model is 280 times faster to construct than a model-based ROM. Note that the difference in extraction time can be justified theoretically and is independent of the specific model-based method used. In fact, any model-based ROM method operates on the matrices A , B , C which have order n , whereas the proposed algorithms have computational complexity that is independent of n and depends only on ν . As $\nu \ll n$, the proposed method is faster.

TABLE I
COMPUTATIONAL COMPARISON

Model	Order	Extraction time	Elapsed time
FOM (nonlinear)	3402	-	1268.26s
FOM (linear)	3402	-	796.31s
ROM	20	28.60s	1.53s
ROM_DD	20	0.10s	1.52s

F. Advanced validation: fault behaviour

Further validation is provided by means of fault simulations. Two fault scenarios are considered:

- 1) A self-clearing fault at bus 14 of the study area occurring at $t = 0.3s$ and cleared after 50ms.
- 2) A fault at bus 8 of the study area occurring at $t = 0.3s$. After 100ms bus 8 is disconnected to protect the rest of the power system.

All the faults are produced by the ‘Three-Phase Fault’ block in the Simulink.

In this section, we reconnect the external area to the study area to verify if the ROM of the external area behaves well not just in isolation, but in the realistic case in which this is interconnected to the rest of the power system. For both cases, the PCC voltage is presented in per-unit (with $V_{base} = 66kV$) while the corresponding relative error is shown in percentage.

1) *Case study 1 (Self-clearing fault)*: A fault occurs at bus 14 of the power system at $t = 0.3s$ and is cleared at $t = 0.35s$. The PCC voltage drops by 19.43% and recovers within 0.15s after the fault is cleared. The top of Fig. 14 shows the PCC voltage of the study area when it is reconnected to the FOM (solid blue lines) and the ROM (dashed red lines) respectively. The PCC voltage of the two models is almost indistinguishable when the bus 14 experiences the fault. The bottom of Fig. 14 shows the respective relative errors (in percentage). The largest relative error occurs in the transient period after the PCC voltage drops or steps (*i.e.* $t = 0.32s$ and $t = 0.36s$). These peak errors are small (0.72% and 0.84%) and decrease to less than 0.4% within 0.1s. We conclude that when a self-clearing

fault occurs at the bus of the power system, the influence on the PCC voltage is recovered precisely by the ROM. Thus, the fault behaviour is fully preserved by the data-driven MOR approach.

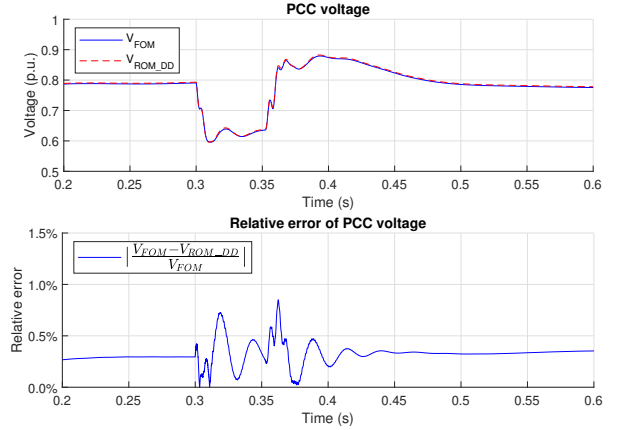


Fig. 14. Top: PCC voltage of the FOM and ROM_DD (data-driven), represented by solid blue and dashed red lines, respectively. Bottom: corresponding relative error.

2) *Case study 2 (Not self-clearing fault)*: A fault occurs at bus 8 of the power system at $t = 0.3s$ and cannot be cleared. Bus 8 is disconnected at $t = 0.4s$ to protect the rest of the power system. This fault results in a voltage drop of 28.04% at the PCC. The top of Fig. 15 shows the PCC voltage of the combined system of the study area and the FOM (solid blue lines) or ROM (dashed red lines), respectively. The bottom of Fig. 15 shows the corresponding relative errors of the PCC voltage with a peak of 1.22% at $t = 0.41s$ and decreasing to less than 0.5% within 0.1s. Since this fault cannot be self-cleared, it is isolated by disconnecting bus 8. Missing the generator at bus 8, the PCC voltage cannot recover and decreases to a smaller value of 0.73pu. This behavior is fully captured by the use of the ROM in place of the FOM.

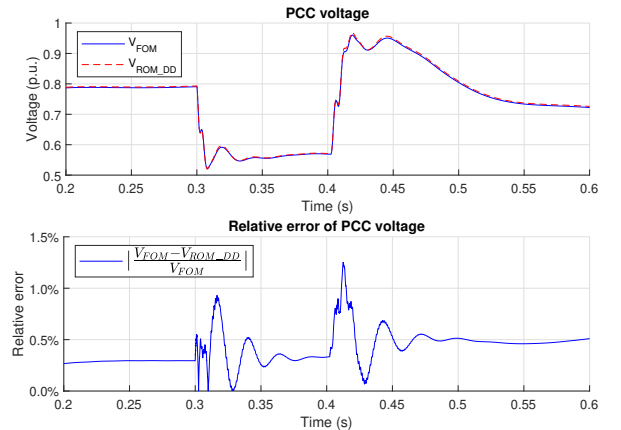


Fig. 15. Top: PCC voltage of the FOM and ROM_DD (data-driven), represented by solid blue and dashed red lines, respectively. Bottom: corresponding relative error.

Moreover, we further evaluate the influence of the ROM on the study area in terms of generator frequency and active

power. We consider the same fault scenario as described in the case study 2. The top of Fig. 16 shows the generator frequency at bus 3 of the study area (with $f_{base} = 50\text{Hz}$). This frequency drops down at $t = 0.3\text{s}$ and finally returns to around 0.996pu after the fault is isolated. The bottom of Fig. 16 shows the active power at bus 3 of the study area (with $P_{base} = 100\text{MW}$). When the fault occurs, the active power steps to more than 1.0pu within 0.1s and finally returns to 0.70pu at the end. Fig. 16 confirms that the performance of the FOM when reconnected to the study area is fully recovered by the ROM.

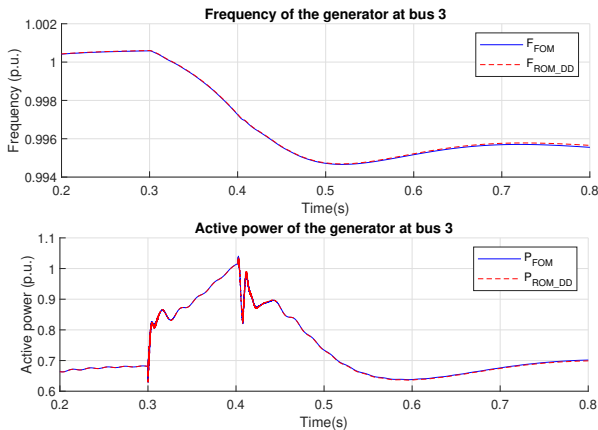


Fig. 16. Top: Frequency of the generator at bus 3. Bottom: Active power of the generator at bus 3. The solid blue and dashed red lines represent the quantities related to the FOM and ROM_DD (data-driven), respectively.

Combining all the simulation results presented in this section, we conclude that by reducing the external area from a complicated FOM to a simple ROM, we considerably reduce the elapsed time of simulations while maintaining high fidelity across a range of different criteria. In addition, the proposed method is robust to measurement noise, it is completely model free and has the advantage of low computational complexity (*i.e.* small extraction time) even in the synthetic data scenario.

V. CONCLUSION

We have presented a data-driven algorithm for the MOR of large-scale wind farms. We presented algorithms to achieve two-sided moment matching for MIMO systems. Unlike other MOR approaches that require full information of the system matrices, the proposed data-driven algorithm is model free, robust to measurement noise and offers low computational complexity to practically overcome the challenges posed by large-scale wind farm. Finally, we have provided extensive simulations that validate the proposed method on a combined model of a 200-turbine wind farm interconnected to the IEEE 14-bus system in terms of Bode plot, eigenvalues, PCC voltage and fault behaviour.

REFERENCES

[1] H. Díaz and C. G. Soares, "Review of the current status, technology and future trends of offshore wind farms," *Ocean Eng.*, vol. 209, p. 107381, 2020.

[2] U.S. Energy Information Administration, "Monthly energy review," <https://www.eia.gov/todayinenergy/detail.php?id=43675>, 2020.

[3] G. Scarciotti, "Low computational complexity model reduction of power systems with preservation of physical characteristics," *IEEE Trans. Power Syst.*, vol. 32, no. 1, pp. 743–752, 2016.

[4] H. R. Ali, L. P. Kunjumammed, B. C. Pal, A. G. Adamczyk, and K. Vershinin, "Model order reduction of wind farms: Linear approach," *IEEE Trans. Sustain. Energy*, vol. 10, no. 3, pp. 1194–1205, 2018.

[5] —, "A trajectory piecewise-linear approach to nonlinear model order reduction of wind farms," *IEEE Trans. Sustain. Energy*, vol. 11, no. 2, pp. 894–905, 2019.

[6] H. R. Ali and B. C. Pal, "Model order reduction of multi-terminal direct-current grid systems," *IEEE Trans. Power Syst.*, vol. 36, no. 1, pp. 699–711, 2020.

[7] V. Akhmatov and H. Knudsen, "An aggregate model of a grid-connected, large-scale, offshore wind farm for power stability investigations—importance of windmill mechanical system," *Int. J. Electr. Power Energy Syst.*, vol. 24, no. 9, pp. 709–717, 2002.

[8] J. Slootweg and W. Kling, "Aggregated modelling of wind parks in power system dynamics simulations," in *2003 IEEE Bologna Power Tech. Conf. Proc.*, vol. 3. IEEE, 2003, pp. 6–pp.

[9] L. M. Fernández, F. Jurado, and J. R. Saenz, "Aggregated dynamic model for wind farms with doubly fed induction generator wind turbines," *Renew. Energy*, vol. 33, no. 1, pp. 129–140, 2008.

[10] L. Fernandez, C. Garcia, J. Saenz, and F. Jurado, "Equivalent models of wind farms by using aggregated wind turbines and equivalent winds," *Energy Convers. Manage.*, vol. 50, no. 3, pp. 691–704, 2009.

[11] M. Ali, I.-S. Ilie, J. V. Milanovic, and G. Chicco, "Wind farm model aggregation using probabilistic clustering," *IEEE Trans. Power Syst.*, vol. 28, no. 1, pp. 309–316, 2012.

[12] J. Zou, C. Peng, H. Xu, and Y. Yan, "A fuzzy clustering algorithm-based dynamic equivalent modeling method for wind farm with dfig," *IEEE Trans. Energy Convers.*, vol. 30, no. 4, pp. 1329–1337, 2015.

[13] P. Wang, Z. Zhang, Q. Huang, N. Wang, X. Zhang, and W.-J. Lee, "Improved wind farm aggregated modeling method for large-scale power system stability studies," *IEEE Trans. Power Syst.*, vol. 33, no. 6, pp. 6332–6342, 2018.

[14] B. Moore, "Principal component analysis in linear systems: Controllability, observability, and model reduction," *IEEE Trans. Autom. Control*, vol. 26, no. 1, pp. 17–32, 1981.

[15] S. Gugercin and A. C. Antoulas, "A survey of model reduction by balanced truncation and some new results," *Int. J. Control*, vol. 77, no. 8, pp. 748–766, 2004.

[16] A. C. Antoulas, *Approximation of large-scale dynamical systems*. SIAM, 2005.

[17] E. J. Grimme, "Krylov projection methods for model reduction," Ph.D. dissertation, University of Illinois at Urbana-Champaign, 1997.

[18] V. Druskin and V. Simoncini, "Adaptive rational krylov subspaces for large-scale dynamical systems," *Syst. & Control Letter.*, vol. 60, no. 8, pp. 546–560, 2011.

[19] D. Chaniotis and M. Pai, "Model reduction in power systems using krylov subspace methods," *IEEE Trans. Power Syst.*, vol. 20, no. 2, pp. 888–894, 2005.

[20] F. D. Freitas, J. Rommes, and N. Martins, "Gramian-based reduction method applied to large sparse power system descriptor models," *IEEE Trans. Power Syst.*, vol. 23, no. 3, pp. 1258–1270, 2008.

[21] J. H. Chow, *Power system coherency and model reduction*. Springer, 2013, vol. 84.

[22] C. Sturk, L. Vanfretti, Y. Chompoobutgool, and H. Sandberg, "Coherency-independent structured model reduction of power systems," *IEEE Trans. Power Syst.*, vol. 29, no. 5, pp. 2418–2426, 2014.

[23] V. Druskin, L. Knizhnerman, and V. Simoncini, "Analysis of the rational krylov subspace and adi methods for solving the lyapunov equation," *SIAM J. Numer. Anal.*, vol. 49, no. 5, pp. 1875–1898, 2011.

[24] S. Gugercin, C. Beattie, and A. Antoulas, "Rational krylov methods for optimal h_2 model reduction," in *17th Int. Symp. Math. Theory Networks Syst. (MTNS)*, vol. 2006, no. 7, 2006, pp. 1665–1667.

[25] G. Scarciotti and A. Astolfi, "Data-driven model reduction by moment matching for linear and nonlinear systems," *Automatica*, vol. 79, pp. 340–351, 2017.

[26] M. F. Shakib, G. Scarciotti, A. Y. Pogromsky, A. Pavlov, and N. van de Wouw, "Time-domain moment matching for multiple-input multiple-output linear time-invariant models," *Automatica*, vol. 152, p. 110935, 2023.

[27] J. Mao and G. Scarciotti, "Data-driven model reduction by moment matching for linear systems through a swapped interconnection," in *2022 Euro. Control Conf. (ECC)*. IEEE, 2022, pp. 1690–1695.

- [28] T. C. Ionescu, "Two-sided time-domain moment matching for linear systems," *IEEE Trans. Autom. Control*, vol. 61, no. 9, pp. 2632–2637, 2015.
- [29] J. Mao and G. Scarciotti, "Data-driven model reduction by two-sided moment matching," *Automatica*, vol. 166, p. 111702, 2024.
- [30] Z. Gong, J. Mao, A. Junyent-Ferré, and G. Scarciotti, "Appendix: Detailed wind farm model and IEEE 14-bus system," <https://github.com/zilong-gong/WindFarmMOR>, 2024.
- [31] A. Junyent Ferré, "Control of power electronic converters for the operation of wind generation," Ph.D. dissertation, Universitat Politècnica de Catalunya, 2011.
- [32] A. Padoan, G. Scarciotti, and A. Astolfi, "A geometric characterization of the persistence of excitation condition for the solutions of autonomous systems," *IEEE Trans. Autom. Control*, vol. 62, no. 11, pp. 5666–5677, 2017.

APPENDIX

A. PROOFS OF THE TECHNICAL RESULTS

In this section, we provide the proofs of the theorems presented in the paper.

Proof of Theorem 1

The minimality of the triple $(L, S, \omega(0))$ implies the excitability of the pair $(S, \omega(0))$. By [32, Lemma 3], there exists a time sequence $\{t_k\}$ with $\lim_{k \rightarrow \infty} t_k = \infty$ such that the time-snapshots \tilde{R}_k is column full rank. The rest of the proof is the same as the proof of [3, Theorem 2]. \square

Proof of Theorem 2

Since Υ is the unique solution of the Sylvester equation (8), we have

$$\begin{aligned} \dot{d} &= \dot{\varpi} + \Upsilon \dot{x} = Q\varpi + Ry + \Upsilon(Ax + Bu) \\ &= Q\varpi + (RC + \Upsilon A)x + \Upsilon Bu = Q(\varpi + \Upsilon x) + \Upsilon Bu \\ &= Qd + \Upsilon Bu \end{aligned} \quad (15)$$

Since the initial condition $x(0) = 0$ and $\varpi(0) = 0$, we have $d(0) = \varpi(0) + \Upsilon x(0) = 0$. Then, the input $u = e_j \delta_0(t)$ yields $\varpi(t) + \Upsilon x(t) = d(t) = e^{Qt} \Upsilon B^j$ for all $t > 0$. Note that system (1) is assumed to be asymptotically stable. Thus, $x(t) \rightarrow 0$ as $t \rightarrow \infty$ yielding

$$\begin{aligned} \Upsilon B^j &= \lim_{t \rightarrow \infty} e^{-Qt} (\varpi(t) + \Upsilon x(t)) \\ &= \lim_{t \rightarrow \infty} e^{-Qt} \varpi(t). \end{aligned}$$

This proves Theorem 2. \square

The robustness claim is a consequence of (13) being the least-square version of (12).

B. MODEL AND PARAMETERS

In this section, we summarise the main parameters used in the simulation. The detailed model and parameters are available in [30].

NOMENCLATURE

Symbols

A	Wind turbine swept surface
C	DC bus capacity
I_t	One-mass wind turbine aggregated inertia
L_l	Inductance of the grid connection impedance
L_q	Generator inductance on q axis
L_d	Generator inductance on d axis
R	Wind turbine radius
V_{DC}^*	DC bus voltage reference value
f^r	Rated frequency
r_s	Resistance of a single phase of the stator windings
r_l	Resistance of the grid connection impedance
U_g^r	Rated collection grid voltage
U_w^r	Rated wind turbine output voltage
v_w	Wind speed
λ_m	Flux linkage per rotating speed unit
ν	Gearbox multiplication ratio
ω_{mn}	Nominal generator speed
ρ	Air density
τ	Time constant of the pitch angle controller

Controller gains

K_p, K_i	gains of the turbine speed controller
K_{pq}, K_{iq}	gains of the generator controller for q axis
K_{pd}, K_{id}	gains of the generator controller for d axis
K_{pg}, K_{ig}	gains of the grid side controller
K_{pc}, K_{ic}	gains of the grid current controller

WIND FARM PARAMETERS

- 1) Wind turbine (see [31, Chapter 2] for details): $c_1 = 1$, $c_2 = 39.52$, $c_6 = 2.04$, $c_7 = 14.47$, $c_3 = c_4 = c_5 = c_8 = c_9 = 0$, $R = 40\text{m}$, $A = 5,026.5\text{m}^2$, $\rho = 1.225\text{kg/m}^3$, $\nu = 90$, $I_t = 4\text{kg} \cdot \text{km}^2$, $\tau = 0.1\text{s}$ and $v_w = 7\text{m/s}$.
- 2) Wind turbine speed controller: $\omega_{mn} = 1,602\text{min}^{-1}$, $K_p = 0.1^\circ \cdot \text{s/rad}$ and $K_i = 0.02^\circ/\text{rad}$.
- 3) Generator: 2 pairs of poles, $r_s = 15\text{m}\Omega$, $\lambda_m = 2.35\text{V} \cdot \text{s/rad}$, $L_q = 0.12732\text{mH}$ and $L_d = 0.12764\text{mH}$.
- 4) Generator vector controller: $K_{pq} = 0.0637\text{V/A}$, $K_{iq} = 7.5\text{V}/(\text{A} \cdot \text{s})$, $K_{pd} = 0.0638\text{V/A}$ and $K_{id} = 7.5\text{V}/(\text{A} \cdot \text{s})$.
- 5) DC bus: $C = 10\text{mF}$ and $V_{DC}^* = 2.6\text{kV}$.
- 6) Grid side system: $r_l = 20\text{m}\Omega$, $L_l = 1\text{mH}$, $U_w^r = 0.97\text{kV}$, $U_g^r = 66\text{kV}$ and $f^r = 50\text{Hz}$.
- 7) Grid side controller: $K_{pg} = 0.6032\text{A/V}$ and $K_{ig} = 14.2122\text{A}/(\text{V} \cdot \text{s})$.
- 8) Grid current controller: $K_{pc} = 0.2803\text{V/A}$ and $K_{ic} = 10\text{V}/(\text{A} \cdot \text{s})$.

C. CODE AVAILABILITY

A demo of the method is available at <https://github.com/zilong-gong/WindFarmMOR>.